Numerical Computations of Transonic Critical Aerodynamic Behavior

Jubaraj Sahu*
U.S. Army Ballistic Research Laboratory, Aberdeen Proving Ground, Maryland 21005-5066

The determination of aerodynamic coefficients by shell designers is a critical step in the development of any new projectile design. Of particular interest is the determination of the aerodynamic coefficients at transonic speeds. It is in this speed regime that the critical aerodynamic behavior occurs and a rapid change in the aerodynamic coefficients is observed. Three-dimensional, transonic, flowfield computations over projectiles have been made using an implicit, approximately factored, partially flux-split algorithm. A composite grid scheme has been used to provide the increased grid resolution needed for accurate numerical simulation of three-dimensional transonic flows. Details of the asymmetrically located shock waves on the projectiles have been determined. Computed surface pressures have been compared with experimental data and are found to be in good agreement. The pitching moment coefficient, determined from the computed flowfields, shows the critical aerodynamic behavior observed in free flights.

I. Introduction

THE flight of projectiles covers a wide range of speeds. The accurate prediction of projectile aerodynamics at these speeds is of significant importance in the early design stage of a projectile. The critical aerodynamic behavior occurs in the transonic speed regime, $0.9 < M < 1.1$ where the aerodynamic coefficients have been found to change by as much as 100%. Of particular interest is the determination of the pitching-moment coefficient since it is used to determine the static stability of the projectile. The critical behavior in this case is usually characterized by a rapid increase in the coefficient followed by a sharp drop. This rapid change in the pitching-moment coefficient can be attributed in part to the complex flow structure and, in particular, to the asymmetrically located shock waves, which exist on projectiles flying at transonic speeds at angle of attack. Computations of three-dimensional flowfields at transonic speeds are thus needed to predict the critical aerodynamic behavior.

In recent years a considerable research effort has been focused on the development of modern predictive capabilities for determining projectile aerodynamics. Numerical capabilities have been developed primarily using Navier-Stokes[1-5] computational techniques and have been used to compute flow over slender bodies of revolution at transonic speeds. Flowfield computations have included both axisymmetric[4] and three-dimensional situations.[1,2,3,5] Initial computations[1-3] did not include the wake or base region of a projectile and, thus, ignored the upstream effect of the base region flow on the afterbody. An axisymmetric base flow code[4] was then developed to compute the entire projectile flowfield including the base region. The base flow code used a flowfield segmentation procedure, which preserved the sharp base corner. This technique was later extended[5] into three dimensions to calculate the pitch plane aerodynamics at transonic speeds. Due to lack of computer resources, only one solution was obtained and reported in Ref. 5. In addition, the calculations in Refs. 1, 2, 3, and 5 generally did not have sufficient grid resolution due to the lack of adequate computer resources. The availability of supercomputers such as the Cray X-MP/48 with a 128-million-word, solid-state disk device (SSD) and the Cray 2 allows for the increased grid resolution, which is needed for accurate computations of three-dimensional transonic flows.[6]

The numerical scheme plays an equally important role for accurate predictions of transonic flows. All the calculations in Refs. 1-5 were made using the compressible, thin-layer, Navier-Stokes equations, which were solved using the implicit Beam and Warming central finite difference scheme.[7-9] Such schemes require artificial dissipation to be added to control numerical oscillations. Upwind schemes can have several advantages over central difference schemes including natural numerical dissipation and better stability properties. The numerical scheme used here is an implicit scheme based on flux-splitting[10] and upwind spatial differencing in the streamwise direction.

Other factors that have direct impact on the three-dimensional numerical simulation are the geometric complexity and efficient management of large three-dimensional data sets. These factors make it necessary to develop zonal or patched methods where a large three-dimensional problem is divided into a number of smaller problems. Each smaller piece is then solved separately. The breakup of the large data base can be achieved in various ways.[11-14] Refs. 11 and 12 are earlier applications where the data base structure follows a pencil format. These numerical calculations, although promising, were based on limited computer resources. Reference 13 shows the development of a chimera grid scheme. This scheme provides multiple regions where communications between grids are done by interpolating in regions of overlap. A blocked grid approach reported by Belk and Whitfield[14] does not require interpolations at the interfaces and has been successfully used to obtain Euler solutions over a wing. The scheme in Ref. 13 is generally complicated since it allows for embedding a block or zone into another. Recently, a simple composite grid scheme[15] has been developed where a large single grid was partitioned into smaller grids. Each of the smaller problems was solved separately with simple data transfers at the interfaces. The initial results obtained were very promising. The present effort extends the use of this composite grid scheme to include the correct modeling of the base region of a projectile. Three-dimensional viscous flowfields have been computed for two different projectiles over a transonic speed range of $0.8 < M < 1.2$. Computed results show the critical aerodynamic behavior.

Received Aug. 17, 1988; revision received June 3, 1989.

*Aerospace Engineer. Member AIAA.

II. Numerical Method

A. Governing Equations

The three-dimensional, Navier-Stokes conservation equations of mass, momentum, and energy can be represented in nondimensional flux vector form as

$$\partial_\tau \boldsymbol{Q} + \partial_\xi(\boldsymbol{F} + \boldsymbol{F}_v) + \partial_\eta(\boldsymbol{G} + \boldsymbol{G}_v) + \partial_\zeta(\boldsymbol{H} + \boldsymbol{H}_v) = 0 \quad (1)$$

where the independent variable τ is the time and the spatial variables ξ, η, ζ are chosen to map a curvilinear body conforming discretization into a uniform computational space. Here $\boldsymbol{Q}$ contains all the dependent variables $[\rho, \rho u, \rho v, \rho w, e]^T$ and $\boldsymbol{F}$, $\boldsymbol{G}$, and $\boldsymbol{H}$ are the inviscid fluxes. The flux terms $\boldsymbol{F}_v$, $\boldsymbol{G}_v$, and $\boldsymbol{H}_v$ contain the viscous derivatives. The conservative form of the equations is used to capture the Rankine Hugoniot shock jump relations as accurately as possible.

For body conforming coordinates and high Reynolds number flow where ζ is the coordinate away from the surface, the thin-layer approximation can be made in the ζ direction. The governing equations can then be written as

$$\partial_\tau \boldsymbol{Q} + \partial_\xi \boldsymbol{F} + \partial_\eta \boldsymbol{G} + \partial_\zeta \boldsymbol{H} = Re^{-1}\partial_\zeta \boldsymbol{S} \quad (2)$$

Here the viscous terms in ζ have been collected into the vector $\boldsymbol{S}$ and the nondimensional reciprocal Reynolds number is extracted to indicate a viscous flux term. The viscous terms in ξ and η directions are neglected.

In differencing these equations, it is often advantageous to difference about a known-base solution denoted by the subscript 0 as

$$\begin{aligned}\delta_\tau(\boldsymbol{Q} - \boldsymbol{Q}_0) + \delta_\xi(\boldsymbol{F} - \boldsymbol{F}_0) + \delta_\eta(\boldsymbol{G} - \boldsymbol{G}_0) + \delta_\zeta(\boldsymbol{H} - \boldsymbol{H}_0) \\ - Re^{-1}\delta_\zeta(\boldsymbol{S} - \boldsymbol{S}_0) = -\partial_\tau \boldsymbol{Q}_0 - \partial_\xi \boldsymbol{F}_0 - \partial_\eta \boldsymbol{G}_0 - \partial_\zeta \boldsymbol{H}_0 \\ + Re^{-1}\partial_\zeta \boldsymbol{S}_0 \end{aligned} \quad (3)$$

where δ indicates a general difference operator, and ∂ is the differential operator. If the base state can be properly chosen, the differenced quantitatives can have smaller and smoother variation and therefore less differencing error. The freestream is used as a base solution in the present formulation.

B. Implicit Finite Difference Algorithm

The implicit, approximately factored scheme for the thin-layer Navier-Stokes equations that uses central differencing in the η and ζ directions and upwinding in ξ is written in the form

$$\begin{aligned}&[I + h\delta_\xi^b(\boldsymbol{A}^+)^n + h\delta_\zeta \boldsymbol{C}^n - hRe^{-1}\bar{\delta}_\zeta J^{-1}\boldsymbol{M}^n J - D_i|_\eta] \\ &\times [I + h\delta_\xi^f(\boldsymbol{A}^-)^n + h\delta_\eta \boldsymbol{B}^n - D_i|_\eta]\Delta\boldsymbol{Q}^n \\ &= -\Delta t\{\delta_\xi^b|(\boldsymbol{F}^+)^n - \boldsymbol{F}_\infty^+ + \delta_\xi^f|(\boldsymbol{F}^-)^n - \boldsymbol{F}_\infty^+ \\ &+ \delta_\eta(\boldsymbol{G}^n - \boldsymbol{G}_\infty) + \delta_\zeta(\boldsymbol{H}^n - \boldsymbol{H}_\infty) - Re^{-1}\bar{\delta}_\zeta(\boldsymbol{S}^n - \boldsymbol{S}_\infty)\} \\ &- D_e(\boldsymbol{Q}^n - \boldsymbol{Q}_\infty)\end{aligned} \quad (4)$$

where $h = \Delta t$, and the freestream base solution is used. Here δ is typically a three-point, second-order, accurate, central-difference operator, $\bar{\delta}$ is the midpoint operator used with the viscous terms, and the operators δ_ξ^b and δ_ξ^f are backward and forward three-point difference operators. The flux vector $\boldsymbol{F}$ has been split into $\boldsymbol{F}^+$ and $\boldsymbol{F}^-$ according to its positive and negative eigenvalues. The matrices $\boldsymbol{A}$, $\boldsymbol{B}$, $\boldsymbol{C}$, and $\boldsymbol{M}$ result from local linearization of the fluxes about the previous time level. Here J denotes the Jacobian of the coordinate transformation. Dissipation operators, D_e and D_i are used in the central-space differencing directions.[6] The factored, left-side operators require inversion of tridiagonal matrices with 5×5 blocks. This two-factor implicit scheme has been vectorized and can be readily multitasked in planes of ξ = constant.

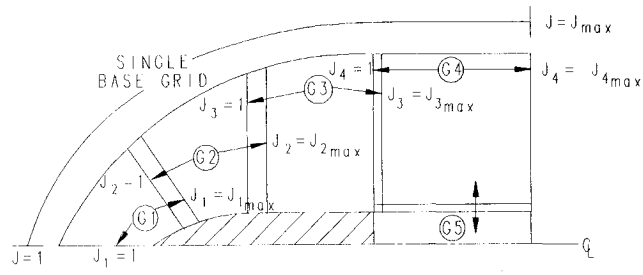

Fig. 1 Schematics of grid partitioning.

C. Composite Grid Scheme

In the present work, a composite grid scheme[15] has been used where a large single grid is split into a number of smaller grids so that computations can be performed on each of these grids separately. Each of these grids use the available core memory in turn; while the rest are stored on an external disk storage device such as the SSD of the Cray X-MP/48 computer. The Cray 2 supercomputer has the large in-core memory to fit the large single grid. However, for accurate geometric modeling of complex projectile configurations that include blunt noses, sharp-base corners, and base cavities, it is also desirable to split the large data base into a few smaller zones on the Cray 2 as well.

A code developed for a single grid can be made to work for a block grid structure by 1) mapping and storing the information for each grid onto a large memory and 2) supplying interface boundary arrays, pointers, and updating procedures. Consider the situation in Fig. 1 in which the single grid from $J = 1$, $J_{\max}$ is partitioned into four grids (or zones), $G1$ through $G4$. The base region of the projectile is included by adding another zone $G5$. This procedure preserves the actual base corner. This zonal scheme has been modified to allow more than one zone in the wake for accurate modeling of other complicated based configurations including cavities.

The use of a composite or blocked grid scheme requires special care in storing and fetching the interface boundary data, i.e., the communication between the various zones. For the simple partitioning shown in Fig. 1, all subgrid points are members of the original grid. There is no mismatch of the grid points at the interface boundaries and no interpolations are required. This procedure, thus, has the advantage over patched or overset grid schemes, which do need interpolations. The partitioned grid has six interface boundaries, $J_1 = J_{1_{\max}}$, $J_2 = 1$, $J_2 = J_{2_{\max}}$, $J_3 = 1$, $J_3 = J_{3_{\max}}$, and $J_4 = 1$ in the streamwise direction and two interface boundaries in the normal direction between grids $G4$ and $G5$. Data for these planes are to be supplied from the other grids by injecting interior values of the other grid onto the interface boundaries. The details of the data storage, transfer, and other pertinent information such as metric and differencing accuracy can be found in Ref. 15. Further details of differencing accuracy are presented next.

The differencing accuracy near the interfaces is quite important. Three-point backward and forward difference operators are used at the interior points. Near the interface, for example, at $J_2 = J_{2_{\max}} - 1$, a three-point, forward-difference operator cannot be used with one grid point overlap as shown in Fig. 1. The differencing accuracy can be dropped from second order to first order; however, this leads to inaccuracies in the flowfield solution near the interfaces.[15] To maintain second-order accuracy near the interfaces, we difference, for example, $(\partial F/\partial\xi)$ at $J_2 = J_{2_{\max}} - 1$ as

$$\frac{\partial F}{\partial \xi} = \partial_\xi^b(F^+) + \partial_\xi^f(F^-)$$

where ∂_ξ^b is the usual three-point, backward-difference opera-

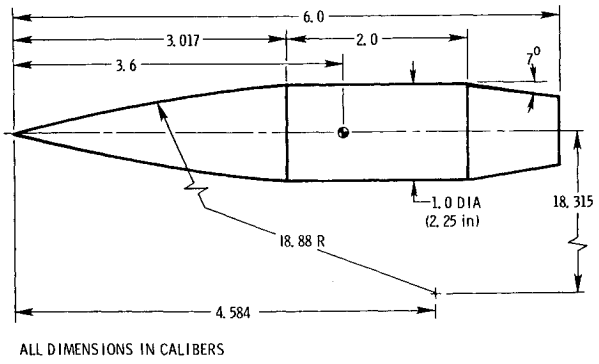

Fig. 2 Model geometry of the SOCBT projectile.

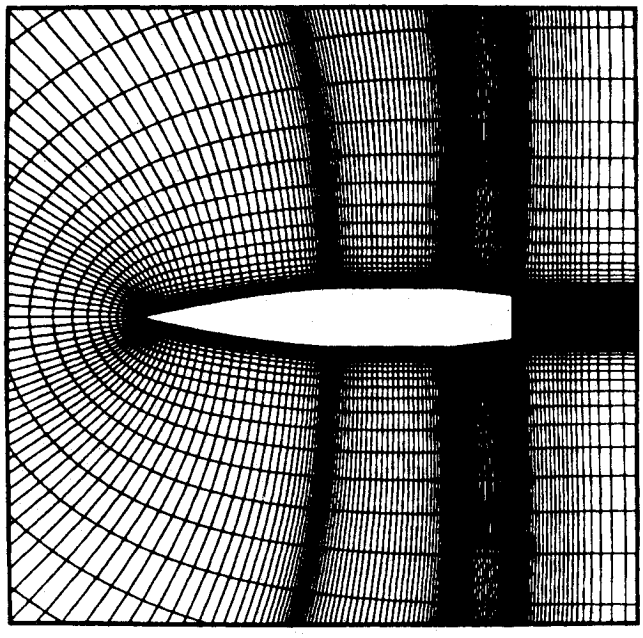

Fig. 3a Longitudinal cross section of the three-dimensional grid.

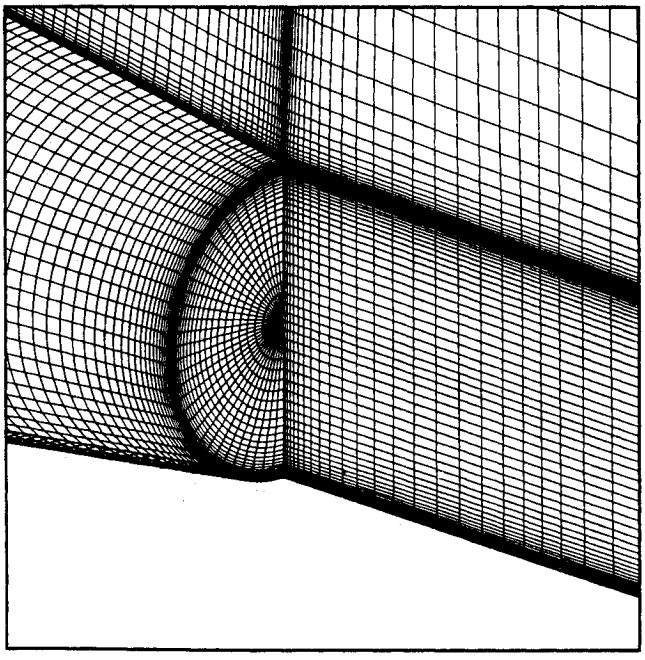

Fig. 3b Expanded view of the base region grid.

tor, and δ_ξ^f is now a central-difference operator, i.e.,

$$\frac{\partial F}{\partial \xi} = \frac{3F_j^+ - 4F_{j-1}^+ + F_{j-2}^+}{2\Delta\xi} + \frac{F_{j+1}^- - F_{j-1}^-}{2\Delta\xi}$$

Near the other interface of grid 2 ($J_2 = 2$), the ∂_ξ^b operator is correspondingly replaced by a central-difference operator, and δ_ξ^f is a usual three-point, forward-difference operator. The planes $J_2 = 1$ and $J_2 = J_{2_{\max}}$ are, of course, boundaries for grid 2 and get their data from interior flowfield solutions from neighboring grids. Second-order accuracy at and near the interfaces is, thus, maintained. The use of central differencing near the interfaces has not adversely affected the stability of the scheme.

III. Model and Computational Grids

The first model used for the computational study presented here is an idealization of a realistic artillery projectile geometry. The experimental model shown in Fig. 2 is a secant-ogive-cylinder-boattail (SOCBT) projectile. It consists of a three-caliber (one-caliber = maximum body diameter), sharp, secant-ogive nose, a two-caliber, cylindrical midsection, and a one-caliber 7-deg conical afterbody or boattail. A similar model was used for the computational studies with the only difference being a 5% rounding of the nose tip. The nose tip rounding was done for computational efficiency and is considered to have little impact on the final integrated forces. Experimental pressure data[16] are available for this shape and were obtained in the NASA Langley 8-ft pressure tunnel using a sting-mounted model. The test conditions of 1 atm supply pressure and 320 K supply temperature resulted in a Reynolds number of 4.5×10^6 based on model length.

The physical grid used for this computation is shown in Figs. 3. Figure 3a shows the longitudinal cross section of the three-dimensional grid, and Fig. 3b shows an expanded view of the three-dimensional, base-region grid. As shown in Fig. 3a, the clustering of grid points near the body surface is done to resolve the viscous boundary layer near the body surface. Grid clustering has also been used in the longitudinal direction near the boattail and the base corners where large gradients in the flow variables are expected. In addition, the composite grid scheme preserves the sharp-base corner. The grid consists

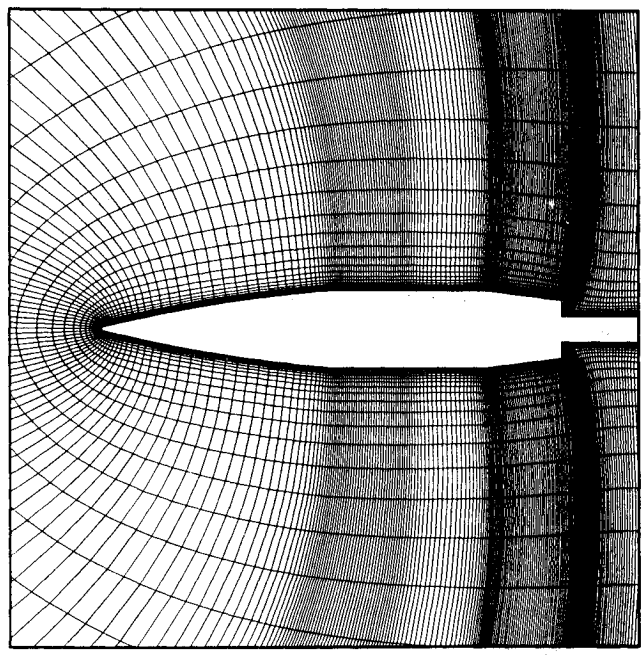

Fig. 4 Grid for the sting-mounted SOCBT projectile.

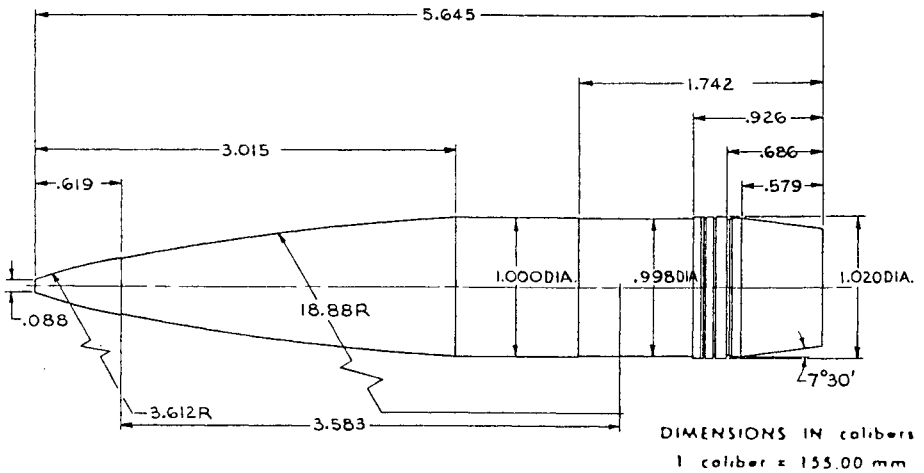

Fig. 5a M549 projectile.

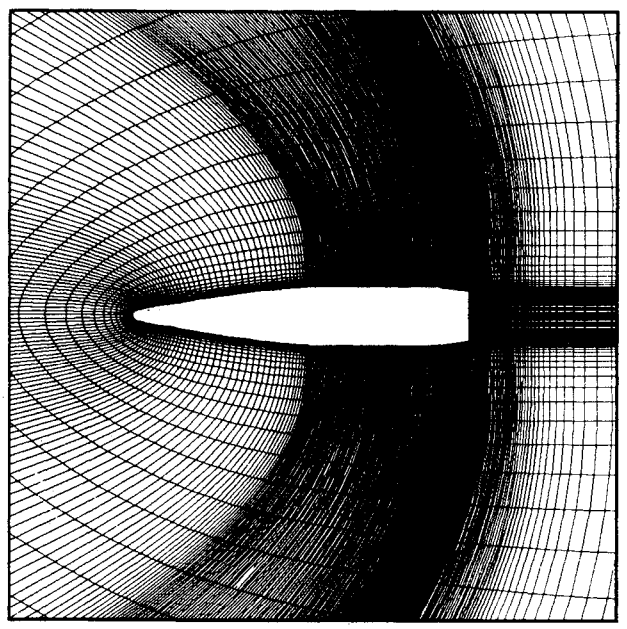

Fig. 5b Longitudinal cross section of the grid for M549 projectile.

of 202 points in the streamwise direction, 36 points in the circumferential direction, and 50 points in the normal direction. This amounts to about 16 million words of storage for the code on the Cray X-MP/48. Only up to 4 million words (Mw) of central-core memory was easily accessible; therefore, the full grid was partitioned into five smaller grids (including a base region grid), each of which would use the core memory in turn while the rest was stored on the SSD device. These computations were performed on the Cray X-MP/48 at the U.S. Army Ballistic Research Laboratory (BRL). Each numerical simulation (includes all partitioned grids) took over 20 hr of computer time.

A second grid, shown in Fig. 4, was obtained to simulate the actual experimental SOCBT configuration, which includes a sting in the base region. This view is again a longitudinal cross section of the three-dimensional grid. The grid is wrapped around the base corner in this case. It consists of 238 points in the axial direction, 39 points in the circumferential direction, and 50 points in the normal direction. Computations on this grid were performed on the Cray 2 computer at BRL using the same code. The computing time for each of these simulations was 20–30 hr. The converged solutions were obtained in 1500–2500 time steps (higher Mach number requiring less iterations).

The second projectile under consideration is the M549 projectile shown in Fig. 5a. This projectile has a short boattail of about ½ a caliber in length. For simplicity, the flat nose was again modeled with nose tip rounding, and the rotating band was eliminated. As shown in Fig. 5a, the rotating band is a small protuberance on the cylindrical afterbody just upstream of the boattail corner. This band engages the rifling in the gun barrel and, thus, imparts spin. The effect of spin on the pitch-plane aerodynamics is rather small. It strongly affects the side force (Magnus force) and moment, which is a subject of further study. Aerodynamic coefficient data[17–19] are available for this configuration and were used for comparison. Computations for this projectile have been made for atmospheric flight conditions. Figure 5b shows an expanded view of the grid around this projectile and shows both the windside and less-side planes. The full grid consists of 298 points in the axial direction, 39 points in the circumferential direction, and 50 points in the normal direction. Calculations for this projectile were performed on the Cray 2 computer at BRL. Each of these calculations took over 30 hr of computer time.

IV. Results

The implicit time marching procedure was used to obtain the desired steady-state result. Initial conditions were free-stream everywhere, and the boundary conditions were updated explicitly at each time step. The solution residual dropped at least three orders of magnitude before converged solutions were obtained. In addition, the surface pressure distributions were checked for time invariance. For the computation of turbulent flow, a turbulence model must be supplied. In the present calculation, a two-layer, algebraic, eddy, viscosity model due to Baldwin and Lomax[20] was used. Results are now presented for two cases: 1) SOCBT projectile with and without sting and 2) M549 projectile.

A. SOCBT Projectile, $0.9 < M_\infty < 1.2$, $\alpha = 4$

Results have been obtained at various transonic speeds for both cases with and without modeling of the sting. Figures 6 and 7 show the Mach contours for the projectile in the windward and lee-ward planes. These figures show the expansions at the ogive-cylinder and cylinder-boattail corners. These figures indicate the presence of shock waves on the cylinder and also on the boattail, which typically occur on the projectile at transonic speeds. Sharp shocks are observed on the boattail. These boattail shocks are shown to be longitudinally asymmetric due to the influence of angle of attack. The asymmetry can also be seen in the wake flow behind the bluff base. As the Mach number is increased from 0.94 to 0.96 and then to 0.98, the shocks become stronger and move towards the base of the projectile. At higher transonic speeds past the speed of sound

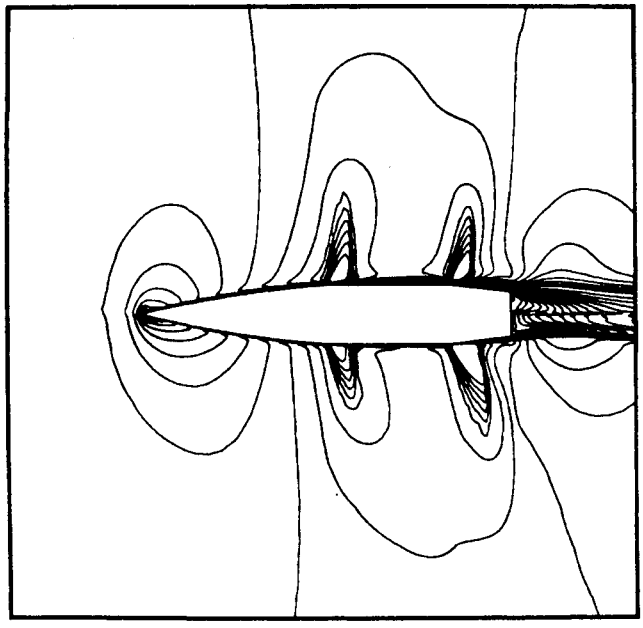

Fig. 6a Mach contours, SOCBT projectile, $M_\infty = 0.94$, $\alpha = 4$ deg.

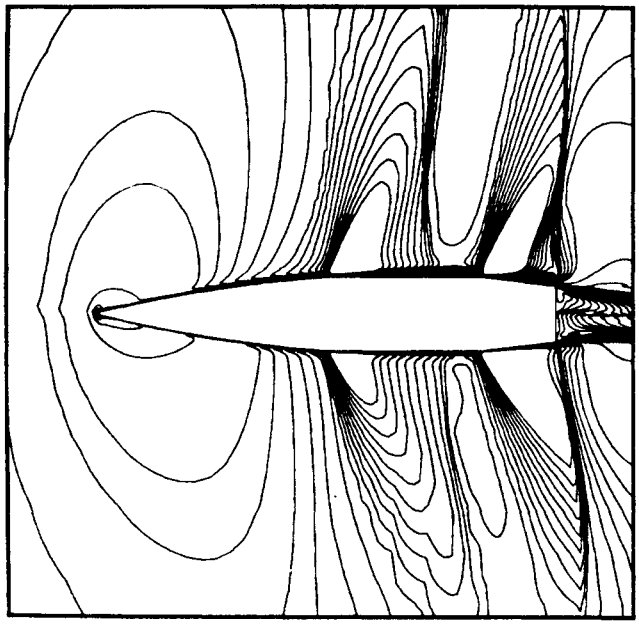

Fig. 7a Mach contours, SOCBT projectile, $M_\infty = 0.98$, $\alpha = 4$ deg.

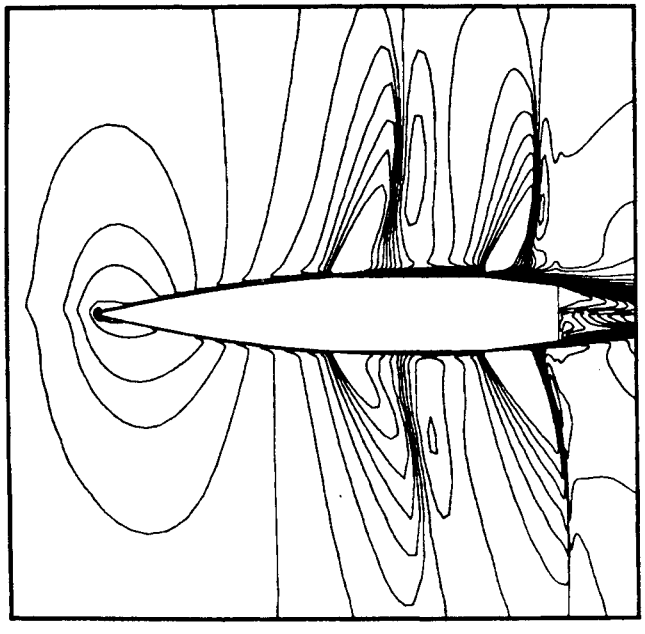

Fig. 6b Mach contours, SOCBT projectile, $M_\infty = 0.96$, $\alpha = 4$ deg.

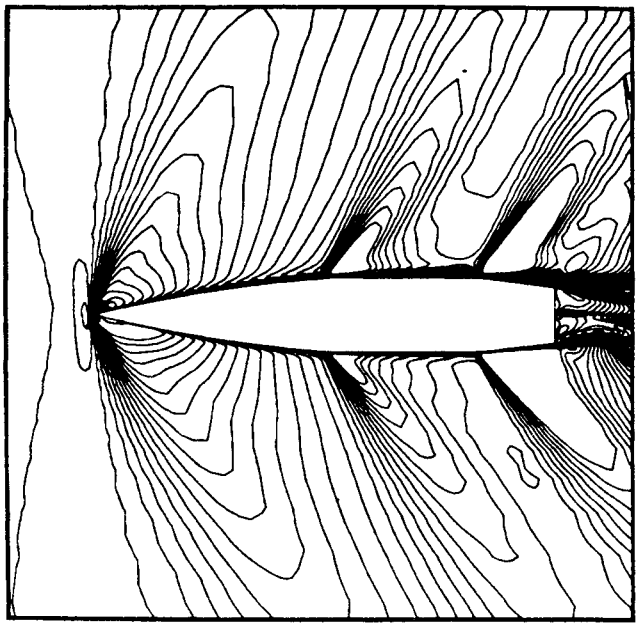

Fig. 7b Mach contours, SOCBT projectile, $M_\infty = 1.1$, $\alpha = 4$ deg.

(see Fig. 7b), these shocks become weak; however, a bow shock forms in front of the nose of the projectile.

Computations have also been made to investigate the effect of the sting on the transonic projectile flowfield. A typical plot of Mach contours for this simulation is shown in Fig. 8a for $M_\infty = 0.96$ and $\alpha = 4$ deg. As expected, the sting has a large effect on the qualitative features of the flowfield in the wake region. An experimentally obtained shadowgraph at the same flow conditions is shown in Fig. 8b. The actual shock-wave position is the front of the structure shown in this shadowgraph. As shown in Figs. 8a and 8b, the agreement between the computation and experiment for the shock-wave positions is good. Figures 9a and 9b show the wind-side and lee-side velocity vectors in the base region for both configurations. Figure 9a is for the case with no sting; whereas Fig. 9b includes the sting in the base region. In both cases, asymmetry in the flowfield can be observed between the wind-side and lee-side. Three pairs of separated flow bubbles can be seen in the near wake for the case of no sting (see Fig. 9a). For the case with sting (see Fig. 9b), one can see the large primary bubble along with a counterrotating small bubble near the junction of the sting and the base. The primary bubble is more elongated on the wind side, and the flow reattaches further downstream of the base.

Figures 10–12 show the surface pressure distributions as a function of the longitudinal position and are compared with experimental data.[16] Figures 10a and 10b show the comparison at $M_\infty = 0.96$ for the wind side and lee side, respectively. Computed results are shown for two grids, one which wrapped around the base corner and the other which did not. As shown in these figures, the computed results are virtually the same for both computations except near the base corner where a small difference can be noticed. The agreement of computed surface pressure with experimental data is good for the wind side. On the lee side, the agreement is good only on the ogive nose, and small discrepancy can be seen on the cylinder as well as on the

boattail. The expansions and recompressions near the ogive-cylinder and cylinder-boattail junctions have been captured. Figures 11a and 11b show the surface pressure distribution for $M_\infty = 0.98$. Computed results are shown for both cases with and without sting for turbulent flow. In the experiment,[16] the model was sting mounted, and no boundary-layer trip was used. Therefore, it is not clear if the flow was laminar or turbulent. Computed results were obtained for the sting-mounted case for both laminar and turbulent-flow conditions and compared with experimental data. Comparison of the pressure on the wind side (see Fig. 11a) shows generally good agreement of the computed pressure with the experimental data. The largest differences between the computed results are seen on the rear part of the boattail where no experimental results are available. The comparison on the lee side (see Fig. 11b) again shows good agreement of the computed result with experimental data for most of the projectile except on the second half of the boattail. As expected, the computed result with no sting has the largest discrepancy. Computed results with sting simulation compare well with experimental data especially for laminar-flow conditions. The difference in computed pressures on the nose and the cylinder between the sting case and no-sting case is a result of different grids used. A typical result at a high transonic speed $M_\infty = 1.1$ is shown in Fig. 12. The agreement of the computed surface pressures with experiment is very good. At this high transonic Mach number,

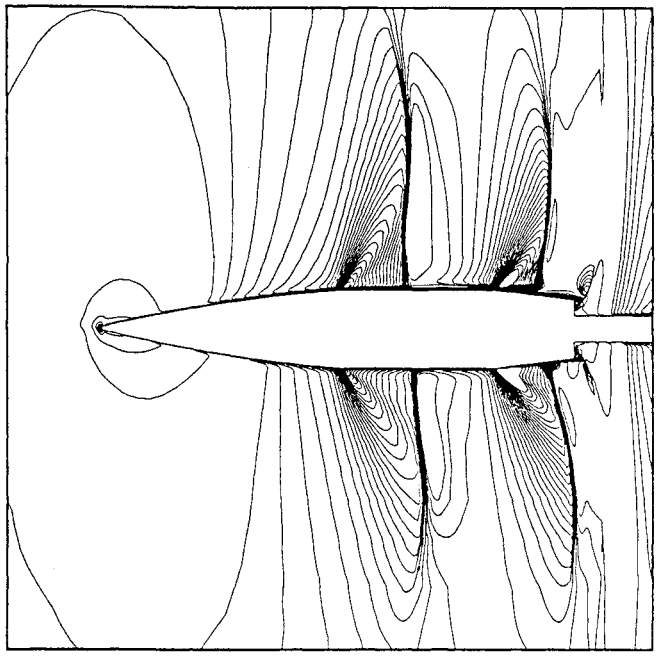

Fig. 8a Computed Mach contours, $M_\infty = 0.96$, $\alpha = 4$ deg, SOCBT projectile (with sting).

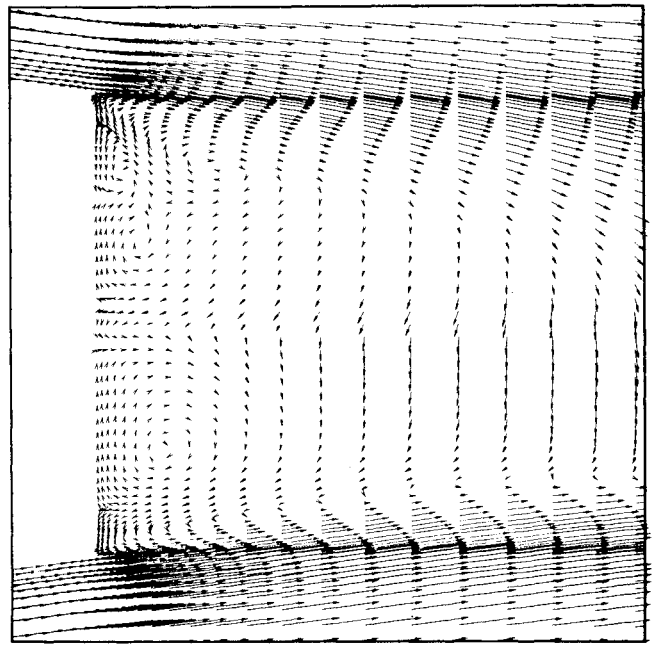

Fig. 9a Velocity vectors in the base region, $M_\infty = 0.96$, $\alpha = 4$ deg, SOCBT projectile (without sting).

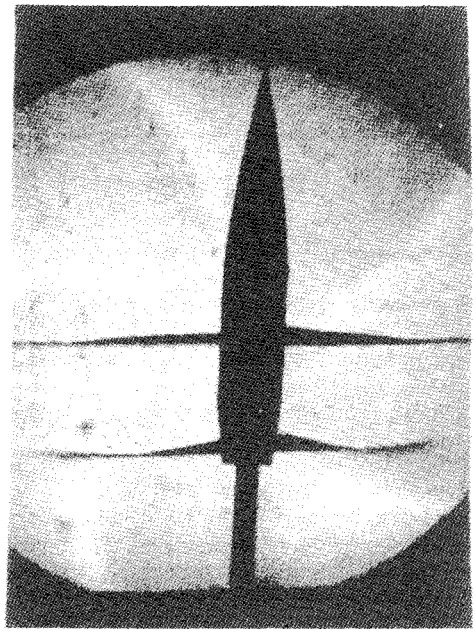

Fig. 8b Experimental shadowgraph, $M_\infty = 0.96$, $\alpha = 4$ deg, SOCBT projectile (with sting).

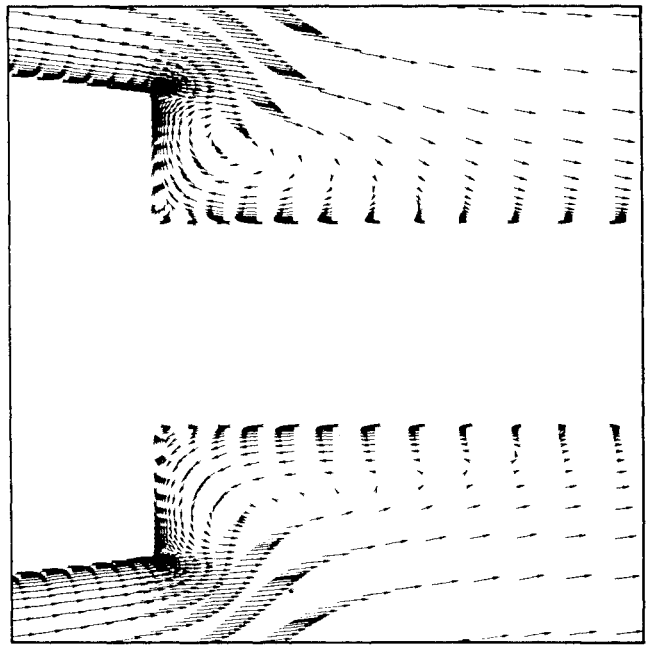

Fig. 9b Velocity vectors in the base region, $M_\infty = 0.96$, $\alpha = 4$ deg, SOCBT projectile (with sting).

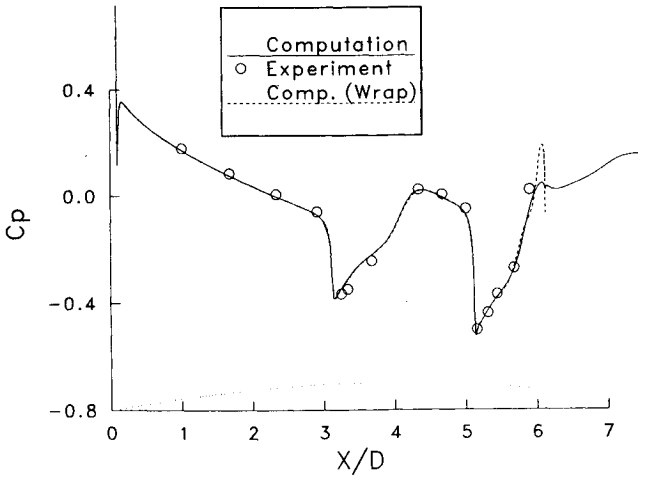

Fig. 10a Longitudinal surface pressure distribution, SOCBT projectile, $M_\infty = 0.96$, $\alpha = 4$ deg, wind side.

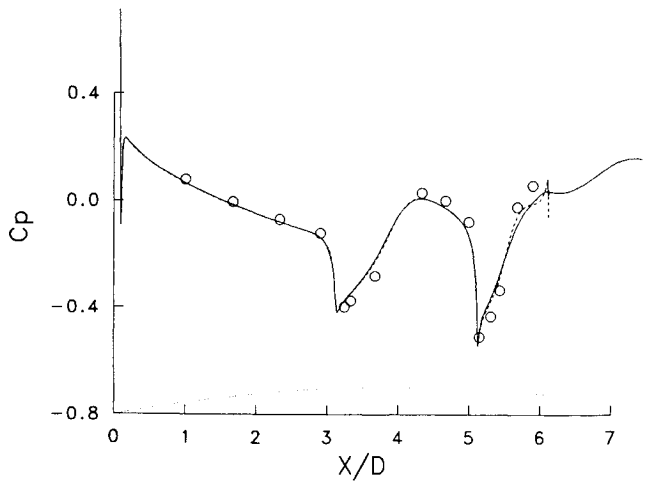

Fig. 10b Longitudinal surface pressure distribution, SOCBT projectile, $M_\infty = 0.96$, $\alpha = 4$ deg, lee side.

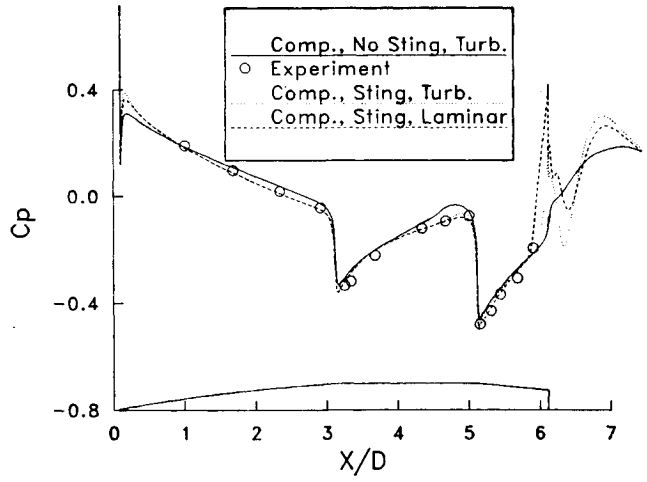

Fig. 11a Longitudinal surface pressure distribution, SOCBT projectile, $M_\infty = 0.98$, $\alpha = 4$ deg, wind side.

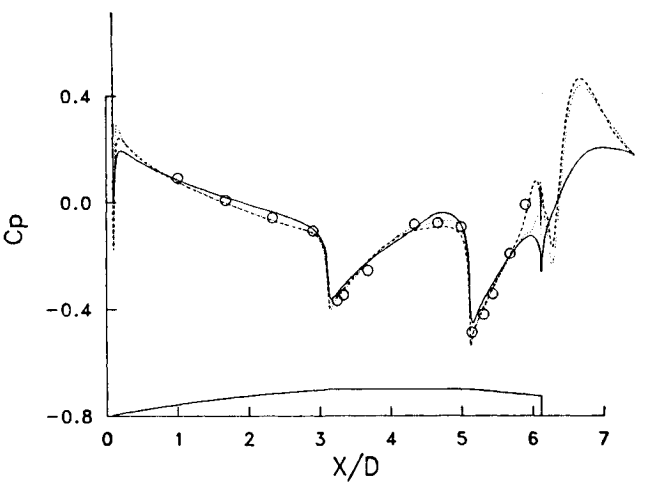

Fig. 11b Longitudinal surface pressure distribution, SOCBT projectile, $M_\infty = 0.98$, $\alpha = 4$ deg, lee side.

the shocks on the cylinder as well as on the boattail are very weak as evidenced by the absence of the sharp rise in pressure in those areas. The expansions and recompressions near the ogive-cylinder and cylinder-boattail junctions can be clearly observed in Fig. 12.

The computed surface pressures have been integrated to obtain the aerodynamic forces and moments. The slope of the pitching moment coefficient (C_{m_α}) is generally of greater concern in projectile aerodynamics since it is the parameter that determines the static stability of the projectile. Figure 13 shows the variation of the slope of the pitching-moment coefficient with Mach number. It clearly shows the critical aerodynamic behavior in the transonic speed regime, i.e., the sharp rise in the coefficient between $M = 0.92$ and 0.96 and its subsequent sharp drop. This is followed by a smooth decrease in the coefficient as the Mach number is increased further. The increase in C_{m_α} between $M = 0.92$ and 0.96 is of the order of 20%, which is a typical value obtained from a number of range tests for similar projectiles.

B. M549 Projectile, $0.7 \leq M_\infty \leq 1.5$, $\alpha = 2$

Numerical computations were made for the M549 projectile at various transonic speeds, $0.7 \leq M_\infty \leq 1.5$ and at angle of attack, $\alpha = 2$ deg. Qualitative features of the flowfield obtained from some of these calculations are shown in Figs. 14 and 15 where Mach number contours have been plotted for

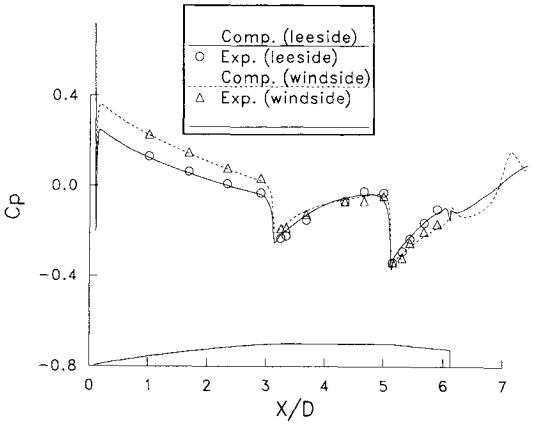

Fig. 12 Longitudinal surface pressure distribution, SOCBT projectile, $M_\infty = 1.1$, $\alpha = 4$ deg.

$M = 0.90$, 0.92, 0.94, and 0.98 for both wind-ward and lee-ward planes. The asymmetry in the wake region flow is obvious from these figures. These figures indicate the development and asymmetric locations of shock waves on the projectile at transonic speeds. At low transonic speeds, for example, at $M = 0.85$ (not shown here), the shock waves just begin to

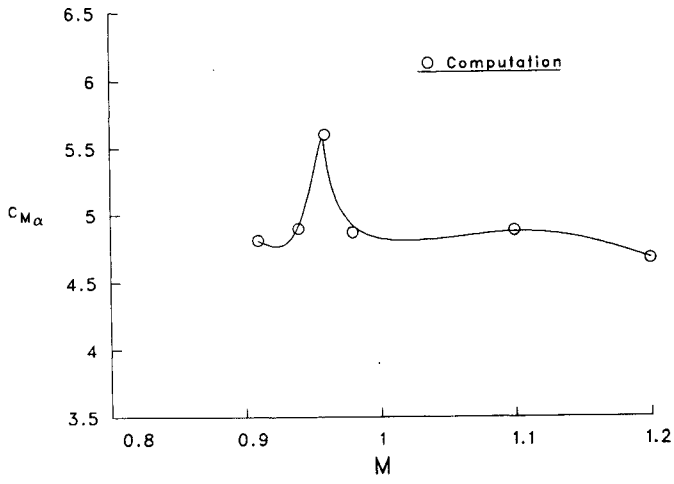

Fig. 13 Slope of pitching moment coefficient, C_{m_α}, vs Mach number, SOCBT projectile.

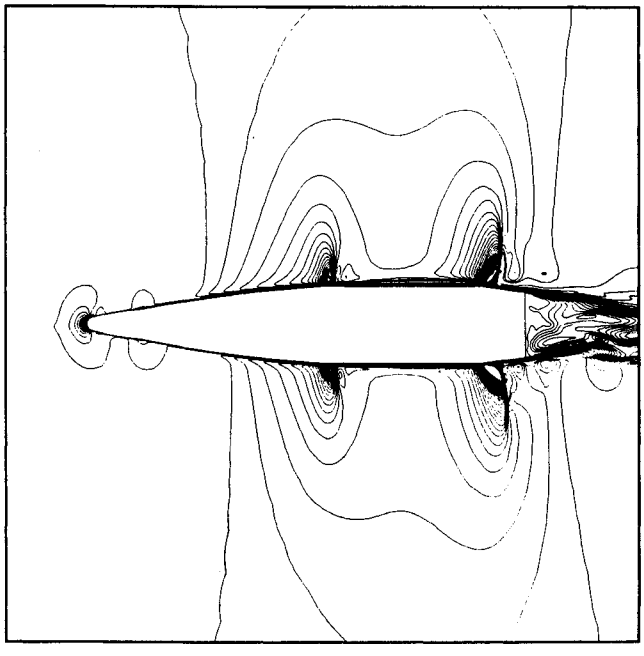

Fig. 14a Mach contours, M549 projectile, $M_\infty = 0.90$, $\alpha = 2$ deg.

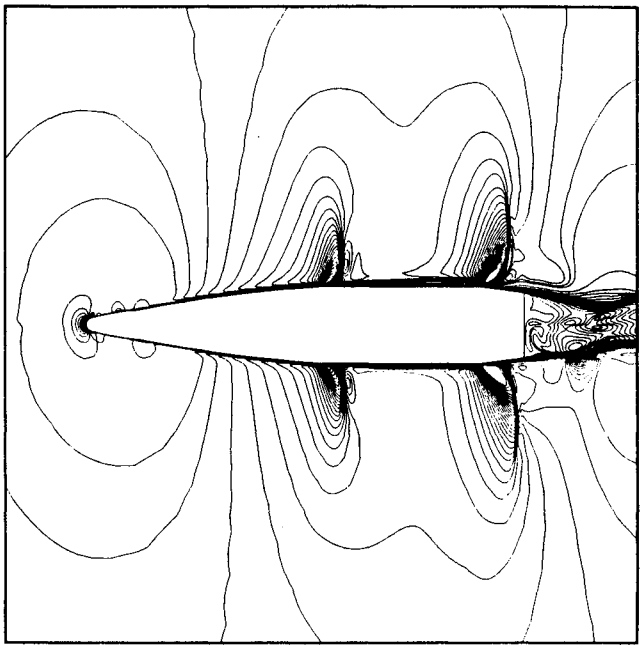

Fig. 14b Mach contours, M549 projectile, $M_\infty = 0.92$, $\alpha = 2$ deg.

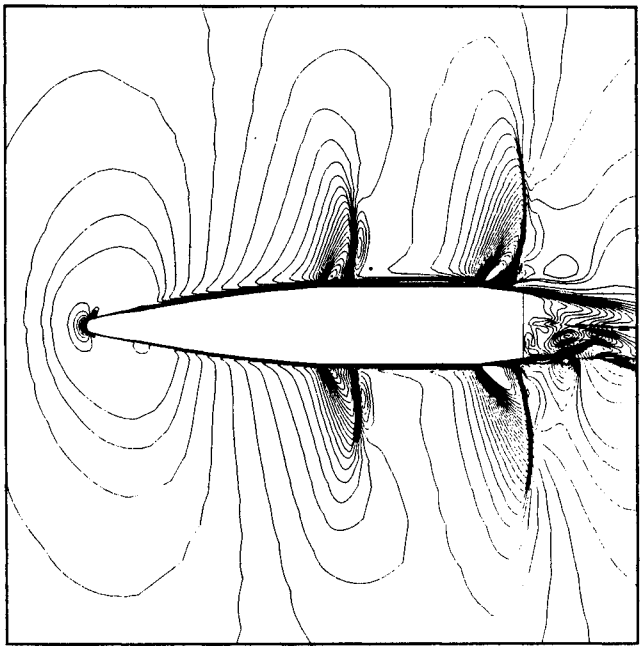

Fig. 15a Mach contours, M549 projectile, $M_\infty = 0.98$, $\alpha = 2$ deg.

form especially near the boattail junction. As the Mach number is increased to $M = 0.90$, the shocks are already formed on the projectile both near the cylinder as well as boattail junctions. The flow expansions at these junctions can also be clearly seen in this figure. The small asymmetry in shock-wave locations can be observed particularly with the boattail shocks. The wind-side shock wave on the boattail is a little closer to the base than its counterpart on the lee side. In addition, these shocks have moved downstream from the boattail junction. As shown in Figures 14b–15b with further increase in Mach number to 0.92, 0.94, and 0.98, the shock waves (both on the cylinder and the boattail) become stronger and gradually move downstream. The asymmetry in the location of the shock waves become more apparent as the Mach number is increased. It is this asymmetry which gives rise to the critical aerodynamic behavior. As seen in Fig. 15b for $M = 0.98$, the shock-wave pattern is complicated and the boattail shocks are located very close to the base corners.

The static aerodynamic coefficients have been obtained from the computed flowfields. As pointed out earlier, the slope of moment coefficients (C_{m_α}) is of primary concern. Figure 16a shows the development of C_m over the projectile for various transonic speeds. Actually, it is the accumulative moment coefficient referenced to the nose and, thus, the value at the end ($X/D = 5.645$) is the final result. The difference in this coefficient over the nose portion is practically negligible for all transonic Mach numbers. The largest effect is seen on the cylinder and boattail sections. The boattail has a dramatic effect as evidenced by the sharp rise in all the curves. Figure 16b shows the C_{m_α} comparison between the computation and the available data.[17-19] Here C_{m_α} is referenced to center of gravity (C.G.) of the projectile. One can clearly see the sharp rise in C_{m_α} between $M = 0.7$ to 0.94, which is followed by the

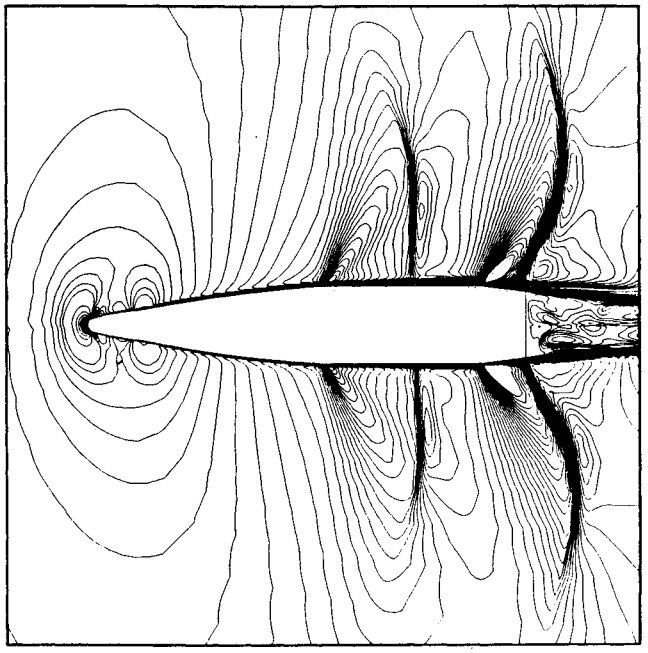

Fig. 15b Mach contours, M549 projectile, $M_\infty = 0.94$, $\alpha = 2$ deg.

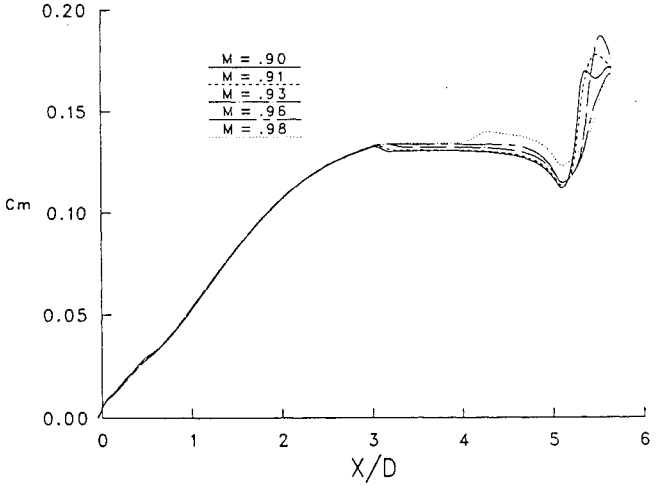

Fig. 16a Development of pitching moment coefficient over the M549 projectile, $\alpha = 2$ deg.

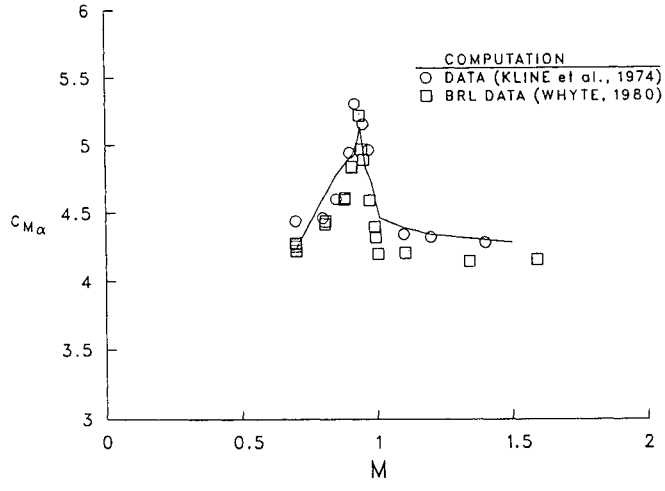

Fig. 16b Slope of pitching moment coefficient, C_{m_α} vs Mach number, M549 projectile.

sharp drop with further increase in Mach number in both the computation and the data. This critical aerodynamic behavior observed in the data is clearly predicted in the computations. Earlier data by Kline et al.[17] is shown in circles and is a compilation of wind-tunnel and free-flight range data. More recent data for this projectile has been obtained from BRL range firings by Whyte et al.[18] and is shown in squares. Each of these data points comes from a six degree of freedom, single-fit procedure. The computed results agree well with the data by Kline et al.[17] for $M > 1.1$. The computed results overpredict Whyte's data by 5–7% at high transonic speeds, $1.0 \leq M \leq 1.4$. Some discrepancy can also be observed at low transonic speeds $M < 0.9$. However, the discrepancy is again of the order of 5–7%. Flight data for transonic region is no better than 7%[19] due to rapid variation of C_{m_α} with Mach number. Thus, the computed results are well within the experimental accuracy at these transonic speeds.

V. Concluding Remarks

In conjunction with a new Navier-Stokes code, a simple composite grid scheme has been developed. This capability allows the use of fine computational grids needed for accurate transonic flow computations on CRAY X-MP/48 or Cray 2 computers. The numerical method uses an implicit, approximately factored, partially upwind (flux-split) algorithm.

The three-dimensional transonic flowfield computations have been made for two projectiles for different flow conditions and angle of attack. The computed flowfields show the development of the asymmetrically located shock waves on the projectile at various transonic speeds. For the SOCBT projectile, computed surface pressures have been compared with experimental data and are found to be in good agreement. The slope of the pitching moment coefficient (C_{m_α}), determined from the computed flowfields, shows the critical aerodynamic behavior. The computed C_{m_α} for the M549 projectile has been compared with available data. Again, the computed results show the same critical behavior seen in the data. The discrepancy between the computed result and data is less than 7%.

The results of this research provide the basis for a new capability to compute three-dimensional, transonic flowfields over projectiles. This capability in conjunction with the supercomputers at BRL has led to the first successful prediction of the critical aerodynamic behavior in C_{m_α} of artillery shell at transonic speeds. The next step is the numerical prediction of Magnus force and moment for spinning projectiles at angle of attack. This involves calculations of the full three-dimensional flowfield with no plane of symmetry.

References

[1]Deiwert, G. S., "Numerical Simulation of Three Dimensional Boattail Afterbody Flow Field," *AIAA Journal,* Vol. 19, May 1981, pp. 582–588.

[2]Nietubicz, C. J., Sturek, W. B., and Heavey, K. R., "Computations of Projectiles Magnus Effect at Transonic Velocities," *AIAA Journal,* Vol. 23, No. 7, July 1985, pp. 998–1004.

[3]Nietubicz, C. J., Sahu, J., and Lafarge, R., "Aerodynamic Coefficient Predictions for a Projectile Configuration at Transonic Speeds," U.S. Army Ballistic Research Laboratory, Aberdeen Proving Ground, MD, BRL-MR-3639, Dec. 1987.

[4]Sahu, J., Nietubicz, C. J., and Steger, J. L., "Navier-Stokes Computations of Projectile Base Flow With and Without Base Injection," U.S. Army Ballistic Research Laboratory, Aberdeen Proving Ground, MD, ARBRL-TR-02532, Nov. 1983. (AD A135738); also *AIAA Journal,* Vol. 23, No. 9, Sept. 1985, pp. 1348–1355.

[5]Sahu, J., "Three Dimensional Base Flow Calculation for a Projectile at Transonic Velocity," AIAA Paper 86-1051, May 1986.

[6]Ying, S. X., Steger, J. L., Schiff, L. B., and Baganoff, D., "Numerical Simulation of Unsteady, Viscous, High-Angle-of-Attack Flows Using a Partially Flux-Split Algorithm," AIAA Paper 86-2179, Aug. 1986.

[7]Beam, R., and Warming, R. F., "An Implicit Factored Scheme for the Compressible Navier-Stokes Equations," AIAA Paper 85-1815-CP, Aug. 1985.

[8]Steger, J. L., "Implicit Finite Difference Simulation of Flow

About Arbitrary Geometries with Application to Airfoils," *AIAA Journal,* Vol. 16, No. 4, July 1978, pp. 679–686.

[9]Pulliam, T. H., and Steger, J. L., "On Implicit Finite-Difference Simulations of Three-Dimensional Flow," *AIAA Journal,* Vol. 18, No. 2, Feb. 1980, pp. 159–167.

[10]Steger, J. L., and Warming, R. F., "Flux Vector Splitting of the Inviscid Gasdynamic Equations with Application to Finite-Difference Methods," *Journal of Computational Physics,* Vol. 40, No. 2, 1981, pp. 263–293.

[11]Lomax, H., and Pulliam, T. H., "A Fully Implicit Factored Code for Computing Three Dimensional Flows on the ILLIAC IV, Parallel Computations," *G. Rodrigue Ed.,* Academic Press, New York, 1982, pp. 217–250.

[12]Deiwert, G. S., and Rothmund, H., "Three-Dimensional Flow Over a Conical Afterbody Containing a Centered Propulsive Jet: A Numerical Simulation," AIAA Paper 83-1709, 1983.

[13]Benek, J. A., Steger, J. L., Dougherty, F. C., and Buning, P. G., "A Three-Dimensional Chimera Grid Embedding Technique," AIAA Paper 85-1523, July 1985.

[14]Belk, D. M., and Whitfield, D. L., "Three-Dimensional Euler Solutions on Blocked Grids Using an Implicit Two-Pass Algorithm," AIAA Paper 87-0450, Jan. 1987.

[15]Sahu, J., and Steger, J. L., "Numerical Simulation of Three Dimensional Transonic Flows," AIAA Paper 87-2293, Aug. 1987.

[16]Kayser, L. D., and Whiton, F., "Surface Pressure Measurements on a Boattailed Projectile Shape at Transonic Speeds," U.S. Army Ballistic Research Laboratory, Aberdeen Proving Ground, MD, AR-BRL-MR-03161, March 1982 (AD A113520).

[17]Kline, R., Herrman, W. R., and Oskay, V., "A Determination of the Aerodynamic Coefficients of the 155 mm, M549 Projectile," Picatinny Arsenal, Dover, NJ, Technical Rpt. 4764, Nov. 1974.

[18]Whyte, R. H., Burnett, J. R., Hathaway, W. H., and Brown, E. F., "Analysis of Free Flight Aerodynamic Range Data of the 155 mm M549 Projectile," U.S. Army Large Caliber Weapon Systems Laboratory, Dover, NJ, ARLCD-CR-80023, Oct. 1980.

[19]Murphy, C. H., private communications, U.S. Army Ballistic Research Laboratory, Aberdeen Proving Ground, MD, Sept. 1988.

[20]Baldwin, B. S., and Lomax, H., "Thin Layer Approximation and Algebraic Model for Separated Turbulent Flows," AIAA Paper 78-257, 1978.